



HAL
open science

Cooperative Brachytherapy Robotic Concept for localized Cancer Treatment under Real-time MRI

Abdelkader Belarouci, Sepaldeep Singh Dhaliwal, Mario Sanz-Lopez, Fabien Verbrugghe, Othman Lakhal, Taha Chettibi, Rochdi Merzouki

► **To cite this version:**

Abdelkader Belarouci, Sepaldeep Singh Dhaliwal, Mario Sanz-Lopez, Fabien Verbrugghe, Othman Lakhal, et al.. Cooperative Brachytherapy Robotic Concept for localized Cancer Treatment under Real-time MRI. IEEE Transactions on Medical Robotics and Bionics, 2022, 4 (3), 10.1109/TMRB.2022.3185796 . hal-03701261

HAL Id: hal-03701261

<https://hal.science/hal-03701261>

Submitted on 21 Jun 2022

HAL is a multi-disciplinary open access archive for the deposit and dissemination of scientific research documents, whether they are published or not. The documents may come from teaching and research institutions in France or abroad, or from public or private research centers.

L'archive ouverte pluridisciplinaire **HAL**, est destinée au dépôt et à la diffusion de documents scientifiques de niveau recherche, publiés ou non, émanant des établissements d'enseignement et de recherche français ou étrangers, des laboratoires publics ou privés.



Distributed under a Creative Commons Attribution - NonCommercial 4.0 International License

Cooperative Brachytherapy Robotic Concept for localized Cancer Treatment under Real-time MRI

Abdelkader Belarouci ¹, Sepaldeep Singh Dhaliwal ², Mario Sanz-Lopez ³, Fabien Verbrughe ⁴, Othman Lakhal ⁵, Taha Chettibi ⁶ and Rochdi Merzouki ⁷

Abstract—Currently, localized cancer treatment is one of the focused research interests of Physicians. Indeed, with the advent of sensor and actuator technologies with the feasibility of integrating multiple systems, treatment and diagnosis have gained more interest in incorporating Magnetic Resonance Imaging (MRI) due to better soft-tissue contrast. In this paper, the authors report the development of the MR-based Cooperative Brachytherapy (CoBra) robot design for in-bore patient prostate intervention, in terms of diagnosis and treatment of localized cancers. The presented CoBra system is characterized by three main MR-compatible components: a suitable leg-support ensuring patient stabilization, a versatile robotized needle guide, and an automated implant driver to deposit precisely radioactive seeds. In fact, ergonomically in-bore needle placement is a challenging problem, whereas the CoBra robot aims to help in in-bore intra-operative intervention under closed-loop control based on imagery feedback. This feedback might be exploited judiciously for tracking online the biological target during changes after needle insertions. Within this framework, the paper discusses the CoBra robot with a focus on kinematics design, modeling, instrumentation, control, and MRI in-bore robot tests, with respect to the adopted clinical workflow. Also, Preliminary experimental results simulating an adaptive prostate LDR-BT under 3 Tesla MRI are given to validate the proposed concept.

Index Terms—Focal therapy, Integrated design, MRI Robot, Prostate cancer, Robotized Prostate Brachytherapy.

I. INTRODUCTION

PROSTATE cancer is the second most commonly diagnosed in men, and 1.3 million new cases were reported in 2018 ¹.

For prostate cancer, commonly used treatment techniques are: *Brachytherapy (BT)*, *External beam radiation therapy*, *Cryotherapy*, *Ablation*, *Prostatectomy*, and *High Intensity Focused Ultrasound (HIFU)*. In the case of BT, it can be carried out as a Low Dose Rate (LDR) or a High Dose Rate (HDR).

Manuscript submitted on September 14, 2021; revised December 13, 2021; revised April 12, 2022. This work has been co-funded by the European regional development Fund under EU Interreg 2 Seas, **Grant CoBra: 2S04-022**. (Corresponding author: Sepaldeep Singh Dhaliwal)

Abdelkader Belarouci, Sepaldeep Singh Dhaliwal, Mario Sanz-Lopez, Fabien Verbrughe, Othman Lakhal, and Rochdi Merzouki are with Centre de Recherche en Informatique, Signal et Automatique de Lille (CRISTAL) UMR CNRS 9189, University of Lille and Centrale Lille Institute, 59650 Villeneuve d'Ascq, France (e-mail: abdelkader.belarouci@univ-lille.fr; rochdi.merzouki@univ-lille.fr).

Taha Chettibi is with the Mechanical engineering Department, University of Blida1, Blida 09000, Algeria, and was a visiting professor at CRISTAL, University of Lille, 59650 Villeneuve d'Ascq, France (e-mail: tahachettibi@gmail.com).

¹<https://www.wcrf.org/dietandcancer/prostate-cancer-statistics/>

In LDR-BT, radioactive implants (isotopes I-125, Pd-103, or Cs-131)² are permanently implanted, whereas in HDR, the source (Ir-192) wire is inserted and retracted back to the HDR afterloader after a specific dwell time³.

Researchers throughout the world have worked to enhance the efficiency, techniques, and procedural workflows and the procedures have evolved with time to be opted as standardized workflow based on the recommendations and reports by task-groups, for example [1]. Transrectal ultrasound imaging (TRUS)-BT is a standardized procedure for prostate BT and is currently being practiced in clinical practice. Similarly, mp-MRI has evolved in recent decades in diagnosis, for example, with the PI-RAD v2⁴, and is currently under clinical investigation for standardized procedural workflows to be followed for treatment too.

In parallel, research teams are also investigating the domain in order to provide robotized solutions for localized treatment and diagnosis. The robotized concepts could serve in various ways, such as precision in lesion targeting and dose placement, a reduced number of needle punctures, and reduced procedural time. Since the first prostate intervention performed under MRI guidance at the Harvard medical school [2], MRI has been explored and under clinical investigation for the last two decades as an alternative to TRUS due to MRI's superior image quality for a variety of anatomical sites.

A detailed survey on MRI robots for prostate intervention can be found in [3], [4], and [5]. DiMaio et al. [6] demonstrated the first robotized concept for prostate intervention under MRI, proving the clinical efficacy of MRI. Stoianovici et al. [7] developed a Mr-Bot, 5 Degree-of-freedom (DOF) pneumatically actuated MR-safe robot using novel *pneustep* motors equipped with optical encoders and limit switches, and demonstrated dummy implant placement in the canine. Bosch et al. [8] performed the first clinical robotized gold fiducial marker placement with a 5 DOF robot actuated using hydraulic and pneumatic actuation. Krieger et al. [9] presented a manually actuated 2 DOF robot with flex-shafts and optical encoders and performed a clinical study with gold fiducial markers' placement via trans-rectal access with 1.1 mm marker placement accuracy. Plante et al. [10] used novel pneumatic muscles actuated by a 4 DOF robot to place robotized gold fiducial markers *in-vivo* for canines under live MRI. Li et al. [11] demonstrated custom brass implant placement in a

²<https://www.aapm.org/meetings/amos2/pdf/59-17318-40500-368.pdf>

³<https://www.elekta.com/brachytherapy/prostate/#sec-treatment-delivery>

⁴<https://www.acr.org/-/media/ACR/Files/RADS/PI-RADS/PIRADS-V2.pdf>

gelatine phantom with a 3 DOF robot-guide and 3 DOF needle module, actuated using piezo motors, and reported an accuracy of implant deposition of 0.98 mm. Jiang et al. [12] presented 5 DOF robot prototype for prostate BT with a piezo ultrasonic motor (USM) and optical encoder sensing. Moreira et al. [13] developed the MIRIAM robot, actuated using a piezo motor with optical incremental rotary encoders for automatic needle placement and trajectory planning. Seifabadi et al. [14] developed a pneumatically actuated robot-guide with optical encoders for tele-operated needle insertion, actuated with the piezo motor. Patel et al. [15] presented a USM actuated robot equipped with incremental encoders and custom optical limit switches for position sensing. Elhawary et al. [16] designed a piezo motor-actuated robot for biopsy with optical encoder sensing and a custom coil for automated targeting using manual trajectory planning. Goldenberg et al. [17] developed an MRI-P robot using USM actuation with optical encoders, demonstrated ablation using automated trajectory for manual needle placement and stated that it is capable of BT needle placement with the integration of an implant loader device. Lin et al. [18] developed a compact 6 DOF robot with USM actuation for prostate intervention. Only a few robots [7], [8], [9], [11], and [19] demonstrated robotized implant or marker placement under MRI guidance, and other systems remain limited needle placement and intervention to be performed by the physician.

Prostate intervention based on MRI guidance can be categorized in different ways depending upon the use of MR-imaging for different stages, for example, stages defined by Wang et al. [20] for LDR/HDR brachytherapy procedures. MRI can be used individually or combined with TRUS for interventional radiotherapy. The prostate intervention incorporating MRI can be (i) in-bore real-time intraoperative (ii) in-bore (not-real time), (iii) out-bore (patient ingress-egress) post-needle-tip verification, and (iv) MRI for TRUS fusion data.

Concerning the robotized systems for prostate intervention, the solutions must take advantage of the MR-Imaging and operate intra-operatively for more precise tumor targeting and reducing the procedural-time. In addition, real-time intraoperative intervention can also get the benefit of a reduction in edema due to the multi-insertion through the perineum as it will reduce the insertion and re-insertion of needles for needle tip-verification, and reduce the overall procedure time. At present, most of the robotized systems are limited to needle positioning with manual needle intervention in an MRI-environment [5]. Limited number of developments actually tested for clinical studies, e.g., [21], [22] (as needle placement for manual biopsy). These developments still left researchers with the motivation to automate solutions for in-bore intraoperative localized treatment or diagnosis [5]. Due to clinical restrictions and ethical issues, it is mandatory to keep the physician in the loop. Therefore, a tele-operative solution can be opted for. Further, for any medical device or equipment for intervention would rely on the needle maneuvering system to target the lesion site. The needle steering concepts are classified by Rossa et al. [23] as (i) Manual assisted (steering & haptics), (ii) Semi-automated steering (Physician in-loop),

TABLE I: MRI robots development toward prostate LDR-BT

Robot/ Author-ref Actuation	Study Type	Kinematic Structure	MRI	Needle		Workflow Provision	implant or GM	Position Sensing
				Inser- tion	Mean Tip accuracy			
Mr-Bot [7] PN	in-vivo canine	Parallel	3 T	Auto	2.02mm	Intraoperative	Dummy Seed	Optical incremental
UMCU [8]	in-vivo Patient	Parallel	1.5T	Man ual	NR	RT Intraoperative	GM	NR
APT-II [9]	in-vivo Patient	Serial	3 T	Man ual	2.7mm	PINV	GM	Optical incremental
MRI-P [17] USM	ex-vivo	Modular Serial	3 T	Man ual	1.1mm	RT Intraoperative	NR	Optical
Elhawary et al.[16] PZ	in-vitro	Serial	1.5T	Auto	2.3mm	RT Intraoperative	X (Biopsy)	Optical incremental
Planic et al.[10] PN	in-vivo canine	Parallel	3 T	Man ual	NR	Intraoperative	GM	NR
Li et al. [11] PZ	in-vitro Gelatine	Parallel	3 T	Auto	0.94mm	RT Intraoperative	Brass Seed	Optical incremental
Seifabadi et al.[14] PN+PZ	in-vitro Gelatine	Parallel	3 T	Man ual	2.5mm	Intraoperative	NR	Optical incremental
Jiang et al. [12] USM	in-vitro Gelatine	Hybrid	3 T	Man ual	1.07mm	Intraoperative	NR	Optical incremental
MIRIAM [13]	ex-vivo (Bovine) USM+PN	Parallel	3 T	Auto	3.9mm	Intraoperative	X (Biopsy)	Optical incremental
Patel et al. [15] USM	in-vitro & in-vivo	Parallel	3 T - 3 T	Man ual	1.5mm - 3.7mm	Intraoperative in-bore	X (Biopsy)	Optical incremental & limit switch
Lin et al. [18] USM	in-vitro	Serial	3 T	-	1.8mm	-	NR	Optical incremental

NR-Not reported, X-Not applicable, GM-Fiducial Gold marker, RT-Real-time
PN-Pneumatic, USM-Ultrasonic motor, PZ-Piezo motor, PINV- Post-implant needle-tip verification

(iii) Fully automated steering.

The demand for surgical robots in brachytherapy is driven by the need to improve implant delivery accuracy, reduce operator-dependence on quality, achieve precise dosimetry, and prevent medical staff from radiation exposure. In contrast, manual LDR-BT techniques, with a rigid template, result in approximately 3-6 mm of implant placement accuracy *in-vivo* [1]. The standard specifications of an image-guided robotic-BT should achieve a spatial accuracy of 1.0 mm (SD = ± 0.5 mm) for implant placement within test phantom conditions and <2 mm under *in-vivo* conditions [1].

The robots developed particularly for prostate brachytherapy, compatible with the MRI environment and with possible extension towards clinical testing, are summarized in Table I, and a detailed classification can be found in [5].

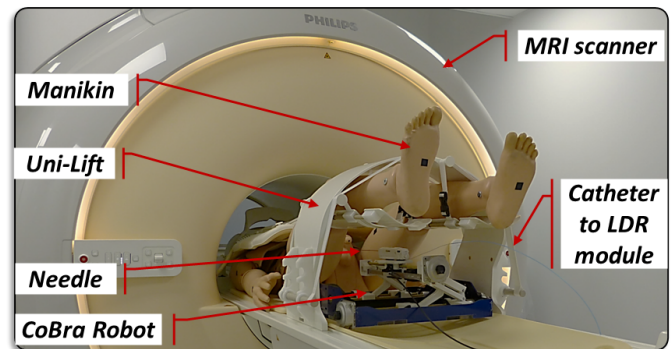


Fig. 1: Environment for automated brachytherapy of the prostate under MRI

In this paper, the authors present a concept for adaptive robotized LDR-BT under real-time MRI [24], [25]. The CoBra robot is an MRI-conditional robot functional in-bore that can be controlled adaptively in a closed-loop under MRI tracking, the setup is shown in Fig. 1. Thus, the concept intends to account for the real-time organ deformations and motions targeting adaptive BT for better accuracy of implant deposition. Also, the paper proposes a technological solution for autonomous and teleoperated adaptive BT under MRI intra-

operatively. To perform the preliminary tests of adaptive-BT, a bio-inspired active prostate phantom (BIP) has been developed [26], emulating the prostate's motions and deformations⁵.

Conventional LDR-BT procedures are performed using TRUS for dose delivery and Computed tomography (CT) scan for post-implant dosage verification. Reviewing the integration of MRI and LDR-BT as discussed in [20], the CoBra concept intends to extend *MRI-Integrated BT* to *MRI-adaptive* real-time intraoperative prostate BT treatment.

From the overall concept, only the robot architecture and the automated implant driver are presented in this work. The paper is organized as follows: Section II describes the robot design with its MR-components, Section III develops the kinematics of the robot, Section IV gives the validation of the kinematic model, Section V validates needle insertion accuracy, section VI explains the automated implant driver, Section VII concerns the robot experiments in MRI, and finally Section VIII conclusion with a discussion of the future steps towards adaptive BT.

II. MRI ROBOT DESIGN

Nowadays, in the medical imaging domain, due to better soft-tissue contrast based on MRI, the latter allows accurate detection of cancer lesions inside the organ volume. MRI is considered superior [27], [28] to classical imaging techniques (CT, ultrasound (US)) for defining the target volume for many brachytherapy sites and adequately visualizing soft tissues such as the prostate base and apex [29], [30]. Also, MRI is well established as the preferred diagnostic image modality for many cancers since soft tissue and tumors are well discriminated [27]. It allows reliable diagnosis and better visualization of carcinomatosis [31]. In image-guided brachytherapy of many cancers, MRI is also considered the preferred imaging modality [27], [28]. Thus, MRI-guided needle intervention is an attractive option for precision targeting and optimal treatment.

However, it brings material compatibility issues for its usage. In the case of robotized system developments for the MRI environment, the conventional electronics can be hazardous near the MRI scanner. This results in stricter safety regulations regarding the use of MRI compared to the US. The selection of material and robot development depends upon high static magnetic field strength, fast switching magnetic gradients, and radio-frequency pulses. MRI necessitates the robot's development with MR compatible materials, actuators, sensors, and shielded electronics, and the placement of the robot and components should follow guidelines based on the magnetic field zones shown in Fig. 2. The robot development for the MRI environment should comply with the ASTM standards (F2503, F2052, F2213, F2182, and F2119), described in [32]. According to F2503-13, only non-conductive components fall under the MR-Safe category.

Considering the robotic developments for prostate intervention, it must be functional in-bore without compromising the imaging and preventing the patient's ingress-egress to avoid prostate position changes. MRI-robot-guide should in

⁵<https://www.youtube.com/watch?v=YZq0mFnCwVY>

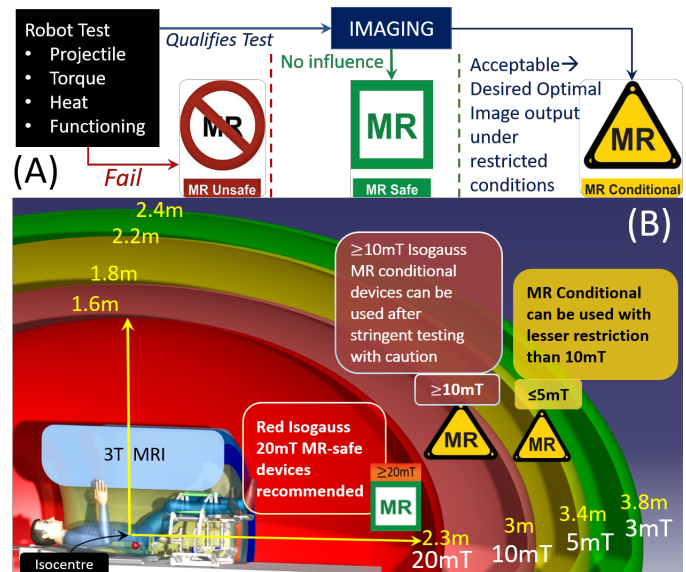


Fig. 2: MRI safety regulations and restrictions for material compatibility for design considerations, iso-gauss based on 3 Tesla (Philips Achieva) [5].

the future be able to perform localized interventions in-bore intraoperatively in real-time to attain the full advantage of MRI guidance in tracking (accurately) moving targets. Considering the in-bore work requirements and patient positing in lithotomy, the authors present the CoBra needle guide robot's detailed design and workspace in this section.

A. Needle Guide Robot Description

The CoBra robot-guide components⁶, both actuators, sensors, and body, have been studied for their compatibility with the high magnetic field (3T), but also for their lack of disturbance of imagery (*i.e.*, absence of artifacts). This is because imaging is used to adaptively control the robot during in-situ interventions. The CoBra needle guide robot (Fig. 3) is a 5 DoF MR-conditional robot actuated with USMs *PSM60N – E2T* (Piezo-Sonic⁷). The robot has a parallel kinematic mechanism (Fig. 4), where its joint-and-loop graph describes 12 revolute, 1 spherical, 2 universal, and 6 prismatic joints. Gray boxes represent actuated joints and white boxes represent passive joints. Underlined joint characters stand for a joint equipped with a position sensor. The compact design of the robot makes it feasible to be placed in-bore beneath the patient's legs, making it ideal for intraoperative prostate needle interventions, where the patient is placed in the lithotomy position. The robot is equipped with MR-conditional absolute encoders (*LAK14 310A Prototype - with a glass* ceramic scale* by NUMERIK JENA GmbH, DE⁸ (Provided by sister company Heidenhain, FR⁹), developed and adapted for the CoBra robot-guide) for position control,

⁶<https://www.youtube.com/watch?v=ZtyOIS-sJ08>

⁷<https://www.piezo-sonic.com/products/general/psm60s-e2t>

⁸<https://www.numerikjena.de/en/linear-encoders/absolute-optical-encoders-from-numerik-jena>

⁹<https://www.heidenhain.fr/>

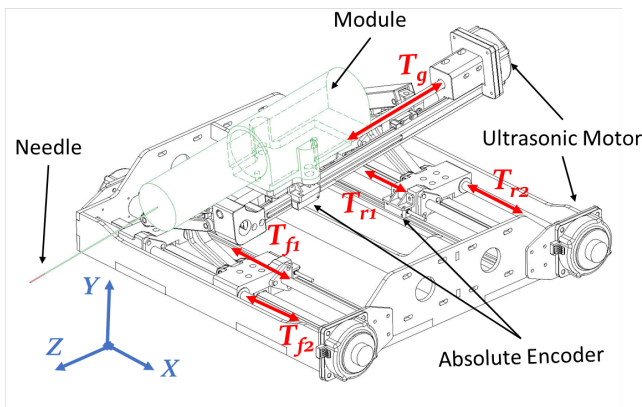


Fig. 3: Description of the CoBra needle guide robot

measuring the linear displacement with a $1.25 \mu\text{m}$ resolution scale. 5 DOFs are attained from 5 linear displacements made by USMs *PSM60N – E2T* (Piezo-Sonic) coupled to a zero backlash lead-screw (made of *Brass*). Each USM is fitted with an incremental encoder with a resolution of 2000 ppr and is associated with a *PSMD – PCC*¹⁰ controller. The USM in the CoBra robot-guide generates a minimum of 0.5 Nm of torque for both high/low velocities ranging from 10 to 120 rpm with the resolution of 0.045° (based on the company's product catalog).

The base of the robot-guide is made of polymethyl-methacrylate (PMMA), the additive manufacturing mechanical parts are made of Polyamide 12 Glass (PA12GS), the linear guides are made of aluminum, and the other parts are non-magnetic stainless-steel, brass, and Iglidur. The mechanical assembly parts are screwed and glued together.

As the CoBra concept intends robot-guide for both BT and biopsy, a common interface is designed on the module platform with a quick-lock mechanism that allows easy mounting and disengagement of biopsy, LDR-BT, or HDR-BT modules for prostate intervention.

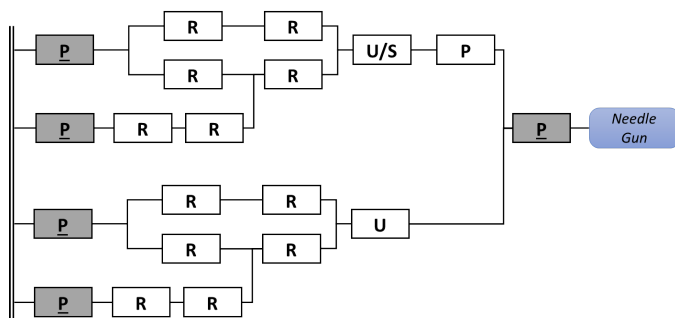


Fig. 4: Joint-and-loop graph of the CoBra needle guide robot

B. Patient In-bore Positioning

In order to access the prostate, there are two main clinical pathways: (i) Trans-perineal access (TP) and (ii) Trans-rectal access (TR), and the choice of prostate access can be related to

the patient's positioning and type of imaging modality. The standard patient positions during clinical procedures are (i) Supine, (ii) Lithotomy, (ii) Semi-lithotomy, (iii) Prone, and (iv) left-lateral decubitus, as detailed in [5]. Further, in the case of MRI in-bore patient placement with the above-mentioned positions, lithotomy is convenient, but determining the prostate position is challenging due to the lack of data with patients in the lithotomy position. The major reason for this can be stated as the patients placed in-bore with aid of custom leg-supports depending upon the availability of facility within the research institute, and MRI bore diameter such as closed bore (60 cm) or wide-bore (≤ 70 cm). In the case of CoBra, the authors opted for the standard commercialized MR-safe leg-support UNI-Lift by NORAS¹¹.

Patient positioning and orientation corresponding to diagnostic images and intraoperative intervention are important for treatment and dosimetry planning. Fedorov et al. [33] state the challenges of using diagnostic scans for targeting during the MR-guided biopsy because the prostate gland deforms due to variations in the patient position (supine vs lithotomy) and the image acquisition (endo-rectal coil vs surface coils). The Uni-Lift by NORAS could be helpful in patient stabilization during diagnostic data acquisition for treatment planning in lithotomy and ensuring the same prostate orientation and position for robotized intervention in-bore intraoperatively.

C. Optimal Robot Work-space

The prostate gland is beneath the TP skin surrounded by critical organs like the bladder, urethra, neurovascular bundles, rectum, called organs-at-risk (OARs), and pubic bone, which makes it challenging to target being soft tissue. In addition, the prostate undergoes deformation and rotation during needle insertion. The robot design was conducted based on the optimal prostate position of the patient in a lithotomy configuration under MRI with Uni-Lift. As explained in the above second paragraph II-B, patient positioning is an important factor for the target organ prostate-related to the influencing factors (movement, displacement, compression, or inflammation). The authors tried to explore the MRI data-sets related to prostate positioning with the patient in lithotomy. Unfortunately, the authors couldn't recover any such MRI data-sets with in-bore lithotomy patient positioning, as in current practice, scans are made in a supine position. The authors cannot account for the Ultrasound-determined prostate position because, unlike the UNI-Lift-supported patient position, the patient's legs are wide-open and raised above with reference to the patient's back. To the authors, it is the most important factor to get an estimation of prostate position in lithotomy (with raised legs, in contrast to supine pose) incorporating UNI-Lift. This information helps in estimating the robot-guide height and target region workspace. Therefore, a volunteer MRI scan of the pelvic region was performed to attain an estimation of prostate position in lithotomy, shown in Fig. 5. The authors intend to state that for the proper dataset, a larger group of real patients should be scanned. In this study, under the current pandemic situation, scanning multiple volunteers was out of

¹⁰<https://www.piezo-sonic.com/products/driver/psmd-pcc>

¹¹<https://www.noras.de/>

points M_r and M_f in space and allows the oblique insertion of the needle (Fig. 8). The robot is built using primarily passive revolute and prismatic joints and active (motorized) helical joints.

A. Forward kinematic model of the rear mechanism

The forward kinematic model (FKM) of the rear side of the CoBra robot describes the coordinates of the vector:

$$\overrightarrow{OM_r} = \overrightarrow{OH_r} + \overrightarrow{H_rB_r} + \overrightarrow{B_rC_r} + \overrightarrow{C_rQ_r} + \overrightarrow{Q_rM_r} \quad (1)$$

Thus, the coordinates of the vector $\overrightarrow{OM_r} = X_{M_r} \cdot \vec{x} + Y_{M_r} \cdot \vec{y}$, can be deduced from the schema of Fig. 9 as follows:

$$\begin{cases} X_{M_r} = T_{r1} + S_r \cdot \cos(\alpha_r) + i_r \\ Y_{M_r} = f_r + a_r + b_r + S_r \cdot \sin(\alpha_r) - \frac{P_r}{2} \end{cases} \quad (2)$$

To determine the forward kinematic model of the rear side of the CoBra robot, a relationship should be obtained between (X_{M_r}, Y_{M_r}) and (T_{r1}, T_{r2}) . For that, the authors have to calculate the variable angle $\alpha_r(t)$, where t is the time variable.

$$\alpha_r = \alpha_{r1} - \beta_{r1} \quad (3)$$

From the triangle $O_{r1}B_rF_r$, the following is deduced:

$$\beta_{r1} = \arctan\left(\frac{\|\overrightarrow{O_{r1}B_r}\|}{\|\overrightarrow{O_{r1}F_r}\|}\right) = \arctan\left(\frac{a_r + b_r}{T_{r2} - T_{r1}}\right) \quad (4)$$

and

$$\begin{aligned} \|\overrightarrow{B_rF_r}\| &= \sqrt{\|\overrightarrow{O_{r1}B_r}\|^2 + \|\overrightarrow{O_{r1}F_r}\|^2} \\ &= \sqrt{(a_r + b_r)^2 + (T_{r2} - T_{r1})^2} \end{aligned} \quad (5)$$

From the triangle $B_rE_rF_r$ and by applying the generalized Pythagorean theorem,

$$\|\overrightarrow{E_rF_r}\|^2 = \|\overrightarrow{B_rE_r}\|^2 + \|\overrightarrow{B_rF_r}\|^2 - 2 \cdot \|\overrightarrow{B_rE_r}\| \cdot \|\overrightarrow{B_rF_r}\| \cdot \cos(\alpha_{r1}) \quad (6)$$

Thus

$$\alpha_{r1} = \arccos\left(\frac{\|\overrightarrow{E_rF_r}\|^2 - \|\overrightarrow{B_rE_r}\|^2 - \|\overrightarrow{B_rF_r}\|^2}{2 \cdot \|\overrightarrow{B_rE_r}\| \cdot \|\overrightarrow{B_rF_r}\|}\right) \quad (7)$$

By combining equations (3), (4), (5), and (7), we obtain :

$$\begin{aligned} \alpha_r &= \arccos\left(\frac{-e_r^2 + l_r^2 + (a_r + b_r)^2 + (T_{r2} - T_{r1})^2}{2 \cdot (l_r \cdot \sqrt{(a_r + b_r)^2 + (T_{r2} - T_{r1})^2})}\right) \\ &\quad - \arctan\left(\frac{a_r + b_r}{T_{r2} - T_{r1}}\right) \end{aligned} \quad (8)$$

The forward kinematic model of the rear mechanism is the following :

$$\begin{cases} X_{M_r} = T_{r1} + S_r \cdot \cos(\alpha_r) + i_r \\ Y_{M_r} = f_r + a_r + b_r + S_r \cdot \sin(\alpha_r) - \frac{P_r}{2} \\ Z_{M_r} = 0 \end{cases} \quad (9)$$

with $T_{r2} \neq T_{r1}$

Using the same analogy, the model of the forward mechanism of the robot can be obtained with the same formulation:

$$\begin{cases} X_{M_f} = T_{f1} + S_f \cdot \cos(\alpha_f) + i_f \\ Y_{M_f} = f_f + a_f + b_f + S_f \cdot \sin(\alpha_f) - \frac{P_f}{2} \\ Z_{M_f} = L_{r_f} \end{cases} \quad (10)$$

with $T_{f2} \neq T_{f1}$ and L_{r_f} is the distance between the base of the forward mechanism and the base frame of the robot.

B. Forward Kinematic Modeling of needle driver CoBra robot

In this case, the authors consider a unit vector $\overrightarrow{W_f}$ of the mobile frame $(M_f, \vec{x}, \vec{y}, \vec{z})$ of the point M_f and defined by two positions M_r and M_f as described in the following equation, Fig. 8:

$$W_t = \frac{\overrightarrow{OM_f} - \overrightarrow{OM_r}}{\|\overrightarrow{OM_f} - \overrightarrow{OM_r}\|} = \begin{pmatrix} X_{M_f} - X_{M_r} \\ Y_{M_f} - Y_{M_r} \\ Z_{M_f} - Z_{M_r} \end{pmatrix} / W \quad (11)$$

Where

$$W = \sqrt{(X_{M_f} - X_{M_r})^2 + (Y_{M_f} - Y_{M_r})^2 + (Z_{M_f} - Z_{M_r})^2}$$

The rotation matrix of the frame $\overrightarrow{W_f}$ of the mobile frame $(M_f, \vec{x}, \vec{y}, \vec{z})$ is a combination of rotations with the X, Y, and Z fixed angles α, β, γ with respect to the initial position [37] as follows:

$${}^{M_f}R^{3 \times 3} = Rz(\gamma) \cdot Ry(\alpha) \cdot Rx(\beta) \quad (12)$$

The rotation angle is $\gamma = 0$ because the pitch motion of the needle driver around the Z axis is not possible with the considered kinematics of the robot.

$${}^{M_f}R^{3 \times 3} = \begin{bmatrix} \cos(\alpha) & \sin(\alpha) \sin(\beta) & \sin(\alpha) \cos(\beta) \\ 0 & \cos(\beta) & -\sin(\beta) \\ -\sin(\alpha) & \cos(\alpha) \sin(\beta) & \cos(\alpha) \cos(\beta) \end{bmatrix} \quad (13)$$

To calculate α, β , the following equality is obtained:

$$\overrightarrow{W_t} = {}^{M_f}R^{3 \times 3} (0 \ 0 \ 1)^T = \begin{pmatrix} \sin(\alpha) \cos(\beta) \\ -\sin(\beta) \\ \cos(\alpha) \cos(\beta) \end{pmatrix} \quad (14)$$

Where :

$$\begin{aligned} \alpha &= -\arctan\left(\frac{W_{tx}}{W_{tz}}\right) \\ \beta &= -\arcsin(W_{ty}) \end{aligned}$$

and

$$\beta \neq \frac{\pi}{2} + k\pi, k \in \mathbb{N}$$

The needle driver is a serial-type manipulator with one translation DoF. The homogeneous transformation matrix H1 of the frame $(M_f, \vec{x}, \vec{y}, \vec{z})$ is described as:

$$H1 = \begin{bmatrix} {}^{M_f}R^{3 \times 3} & \overrightarrow{OM_f} \\ 0 & 1 \end{bmatrix} \quad (15)$$

Now, the homogeneous transformation matrix H2 of the needle tip at the point P_n is described as follows:

$$H2 = H1 \cdot H3(y_0) \cdot H4(Tg + z_0) \quad (16)$$

From the triangle $N_r E_r F_r$, the following is obtained:

$$T_{r2} - X_{Er} = \sqrt{e_r^2 - \left\| \overrightarrow{N_r E_r} \right\|^2} = \sqrt{e_r^2 - (Y_{Er} - f_r)^2} \quad (23)$$

with

$$\begin{aligned} X_{Er} &= X_{Mr} - i_r - (S_r - l_r) (X_{Mr} - i_r - T_{r1}) / S_r \\ Y_{Er} &= Y_{Mr} + \frac{P_r}{2} - (S_r - l_r) \left(Y_{Mr} + \frac{P_r}{2} - f_r - a_r - b_r \right) / S_r \end{aligned}$$

By combining equations (19) and (23), we obtain :

$$\begin{aligned} T_{r2} &= X_{Mr} \frac{l_r}{S_r} - i_r \frac{l_r}{S_r} + T_{r1} \left(1 - \frac{l_r}{S_r} \right) \\ &+ \sqrt{e_r^2 - \left(\frac{l_r}{S_r} (Y_{Mr} + \frac{P_r}{2} - f_r) + \left(1 - \frac{l_r}{S_r} \right) (a_r + b_r) \right)^2} \end{aligned} \quad (24)$$

IV. FORWARD KINEMATIC MODEL VALIDATION

In order to validate the kinematic model, its output was compared with a set of *Optitrack™ Prime 13* cameras run by *Motive™* in a laboratory environment with a reported mean euclidean error of 0.2 mm. Avoidance of delay-based bias was obtained via streaming the tracking data directly into the CoBra needle guide robot, which displays in real-time the full data set, as well as logs the information for later study.

In our tests, the Optitrack markers are placed at the base of the robot to establish a frame reference, as well as the needle driver platform to assess the accuracy of the kinematic model. The nominal values of the robot's geometric parameters are given in (mm): $a_r = 18$; $b_r = 22$; $l_r = 70$; $s_r = 110$; $e_r = 101$; $i_r = 6$; $f_r = 22$; $a_f = 18$; $b_f = 22$; $l_f = 70$; $s_f = 110$; $e_f = 90$; $i_f = 6$; $f_f = 22$; $P_r = 25$; $L_{rf} = 300$; $y_0 = 72$; $z_0 = 380$. The authors applied the same joint input displacements T_{r1} , T_{r2} , T_{f1} , T_{f2} , and T_g of Fig. 10 to the forward kinematic model and to the real robot. The authors compared then the measurements of the needle tip from the Optitrack system and the forward kinematic model (Fig. 11). The Euclidean error is given in Fig. 12 For this curve reconstruction, the mean Euclidean error is about 0.82 mm.

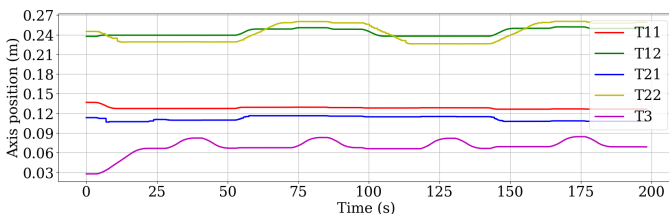


Fig. 10: Desired joint input displacements

A particular source of error is the brass threaded rods used to drive the different prismatic joints, which provoke certain parts of the mechanism to sway slightly during motion. Despite those limitations, the robot shows high repeatability and stability.

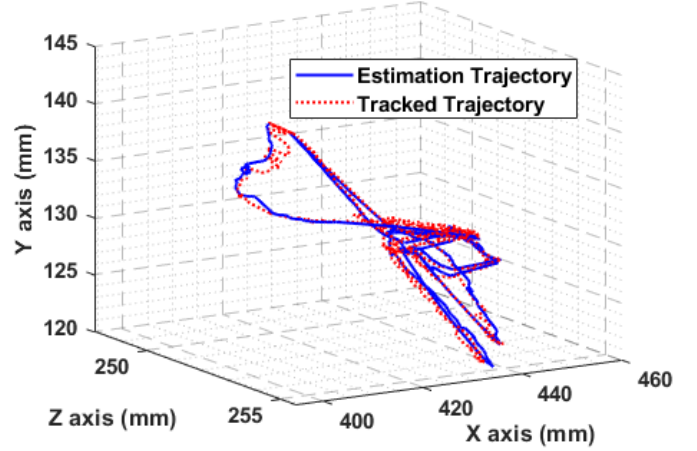


Fig. 11: 3D Trajectory reconstruction of the needle tip

V. INVERSE KINEMATIC MODEL VALIDATION

While the correct robot and needle driver positioning are important steps, the needle insertion is the primary function of such a robot. Thus, the accuracy of the needle tip pose is yet to be quantified during the insertion motion; moreover, deviation during insertion. Two main goals drive this section in order to dimension the final accuracy of the needle tip. In the first stage, the needle vibrates as a result of the mechanical inaccuracies within the robot, as indicated in the previous section, increasing its uncertainty along with its velocity. The other main obstacle is related to the insertion. While inserting through the soft tissue, the needle bends according to its interaction model [38], which would require adaptive correction, which is not considered in this work. The setup for this validation consists of a series of 6 insertions to determine the needle motion repeatability in free air, as well as a block of silicone rubber on which the authors will perform the same motions with insertions of 10 mm depth (Fig. 15). Given that the needle cannot be tracked while performing a full insertion, the target block of silicone has been chosen with dimensions of $80 \times 95 \times 20$ mm and a shore hardness of A30 (593 kPa), intentionally higher than the tissues in the pelvic region, to be able to condensate the efforts and, hence, allow us to observe the eventual needle bending.

Firstly, the tests have been performed in horizontal insertions as it is practiced conventionally. The mean euclidean error of the needle tip position during the insertion is 1.35 mm, with a maximum error of 1.94 mm and a standard deviation of 0.04 mm (Fig.13). This error can be explained by the bending of the needle after physical insertion. Considering the subset of values corresponding to insertion, the mean error rises to 1.76 mm, with a maximum error of 2.05 mm and a standard deviation of 0.136 mm.

Secondly, the tests have been performed in an oblique orientation of 6.3° and -4.4° over the X and Y axis, respectively. The overall mean euclidean error of the needle tip position was determined to be 0.66 mm, with a maximum of 2.83 mm, as can be seen in Fig.14. Considering the subset of values

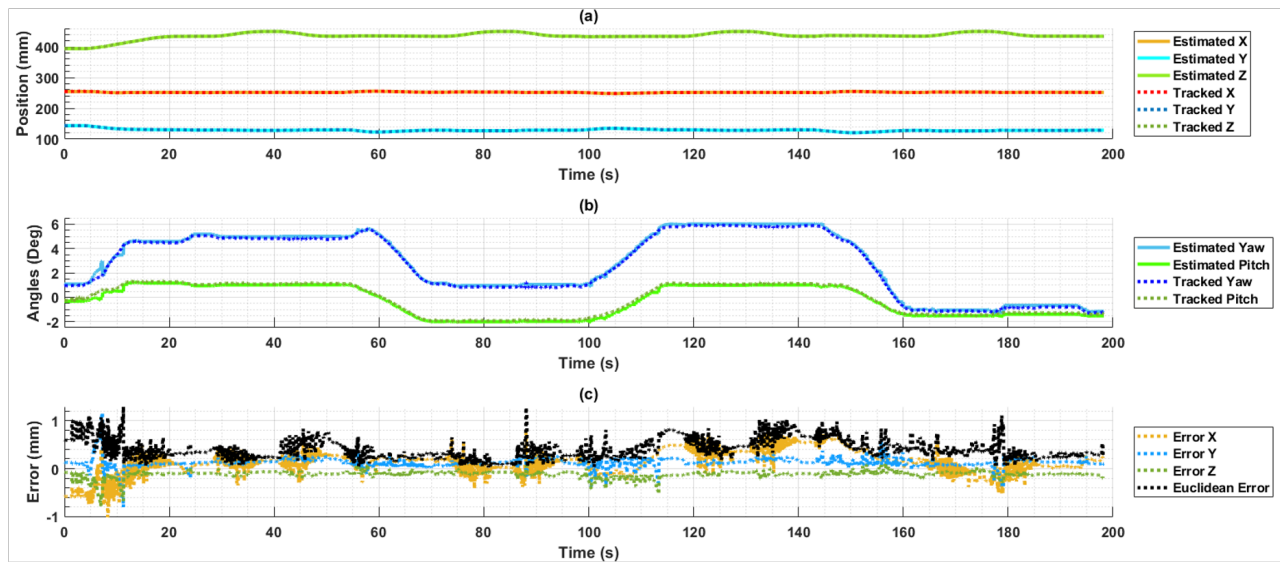


Fig. 12: Needle tip pose reconstruction (a): Tracking and model position values. (b): Tracking and model orientation values (c): the positioning error on the x, y, and z-axis and the Euclidean error.

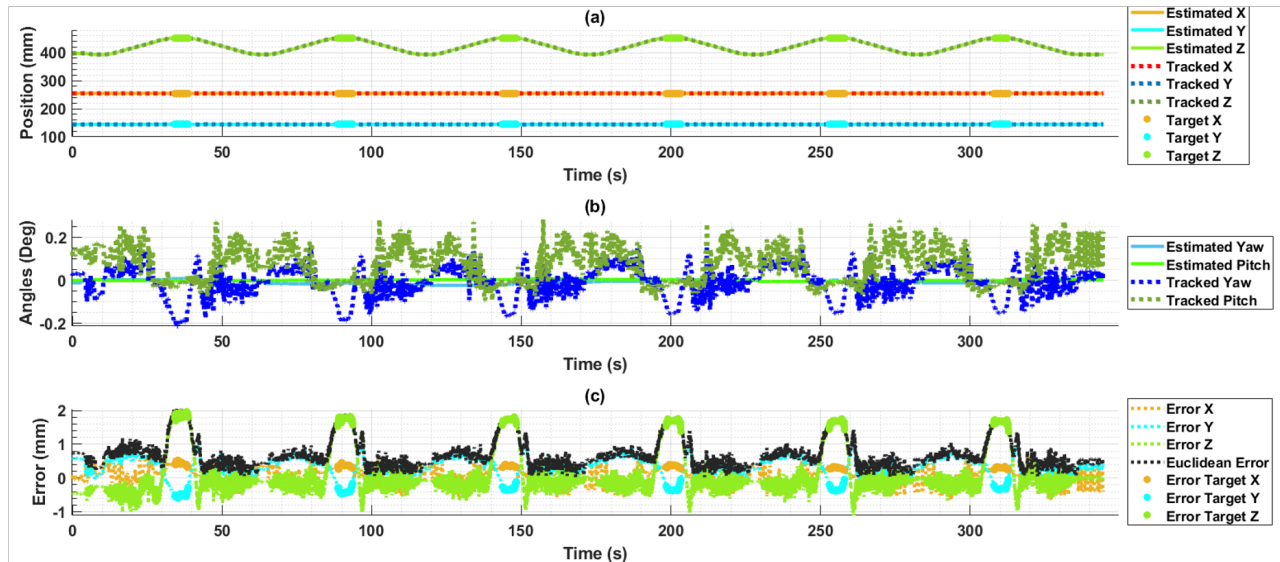


Fig. 13: Analysis of horizontal needle insertions. (a): Tracking and model position values, with the subset for tip location highlighted. (b): Tracking and model rotation values. (c): Position errors and euclidean error.

corresponding to insertion, the mean error reaches 1.57 mm, with a maximum error of 2.01 mm and a standard deviation of 0.216 mm.

Those results show that the inclination has no major impact on the overall accuracy. The presence of the noises from the measures is due to the small vibrations of the Optitrack markers, during the robot motion.

The calibration phase of the model has been performed. It consists of minimizing the mean square error by adapting the robot's geometric parameters to the real robot. Indeed, mechanical backlashes can influence the accuracy of the model and, therefore, the positioning of the needle. To this effect, an algorithm has been developed through convex optimization using the interior-point method on the kinematic model to

adjust the robot's geometric parameters. Fig. 16 describes the calibration steps. From a set of points, the euclidean error is calculated between the data of the tracking system and the estimated values of the forward kinematic model. At the first step and for each iteration, the parameters of the model are randomly varied with a tolerance of ± 0.5 mm. This tolerance is progressively refined in order to converge the squared error towards zero. A performance criterion has been defined at 0.4 mm due to the accuracy of the tracking system. Fig. 17 illustrates the improvement that calibration introduces in a set of samples within the workspace of the CoBra robot. After the model calibration, the mean Euclidean error down to 1.3988mm with a standard deviation of 0.9594mm.

Finally, Fig. 18 illustrates two targets, one identified for

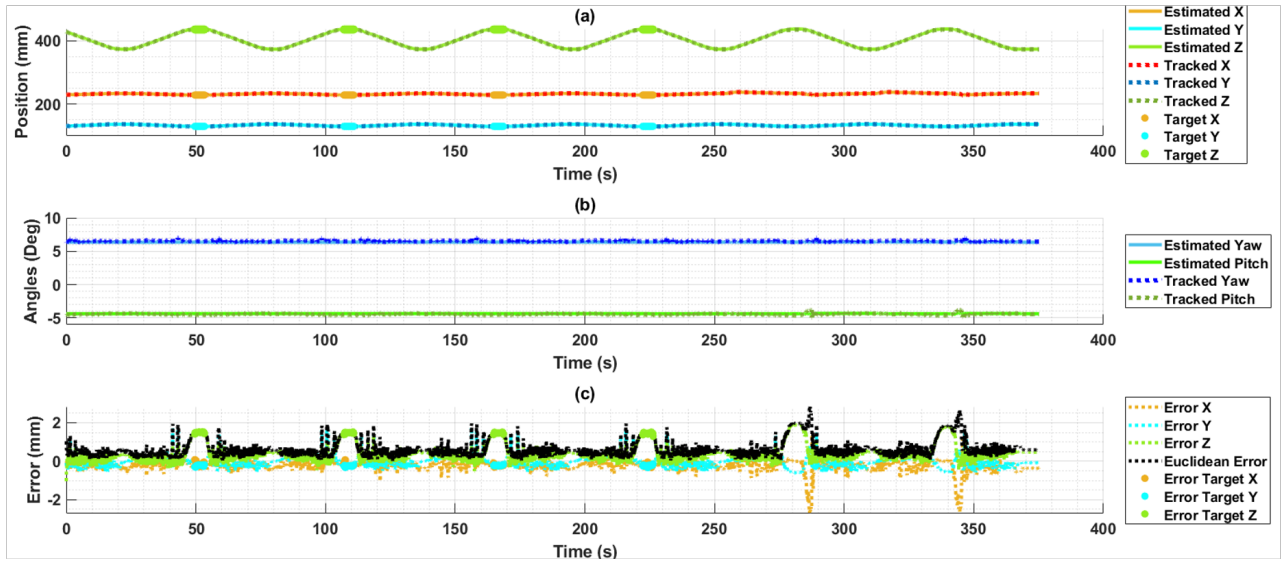


Fig. 14: Tracking data of a series of oblique needle insertions. (a): Tracking and model position values, with the subset for tip location highlighted. (b): Tracking and model rotation values. (c): Position errors and euclidean error.



Fig. 15: Set-up used to determine the accuracy of needle tip pose during the insertion.

horizontal insertion and the other for oblique insertion. For both targets, the position of each implant is determined by the needle tip location, very close to each target, showing the accuracy of the kinematic model after calibration and, moreover, the repeatability performance of the CoBra robot.

VI. AUTOMATED IMPLANT DRIVER

The CoBra concept intends to make the positioning of the implant with an automated driver, saving the implant-loading time and procedural workflow time. In literature [5], concerning an automated implant-loading device, only four concepts [39], [40], [41], and [42] are proposed in the authors' knowledge, and the only one by Patriciu et al. [39] (pneumatic actuated) is compatible under the MRI environment. The CoBra team presents an MR-conditional USM (*Shinsei Corp.* - USR60-E3ET) actuated implant driver equipped with MRI-safe optical sensors (*Micronor* - U-Beam).

The automated implant driver allows the loading of the needle with implants (radioactive seeds, fiducial markers) and depositing (delivery) the implant into the target organ. It is

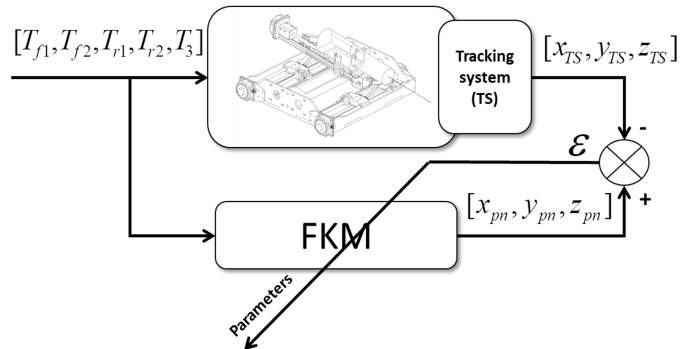
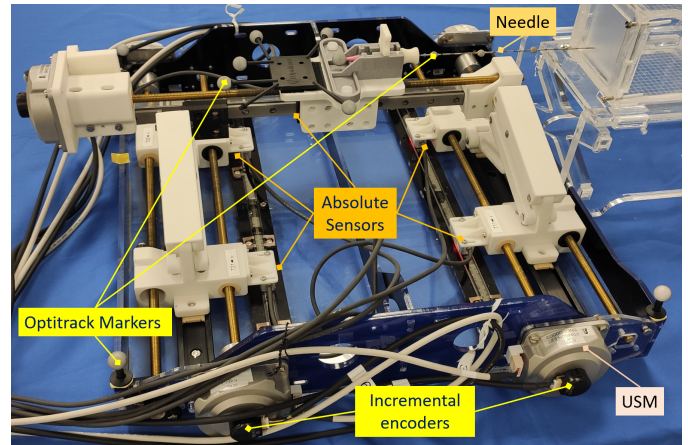


Fig. 16: Model Calibration using Optitrack system.

illustrated in Fig. 19. The system is made of two parts; the first one allows the pre-loading of the implant of 0.8 mm in diameter in the catheter, and the second one is for the routing and deposit of the implant into the target organ.

- 1) **Pre-loading of the Implant:** The system allows the extraction of the implant (4) from the cartridge (3) and its delivery to the catheter inlet (5) using a mandrel (2)

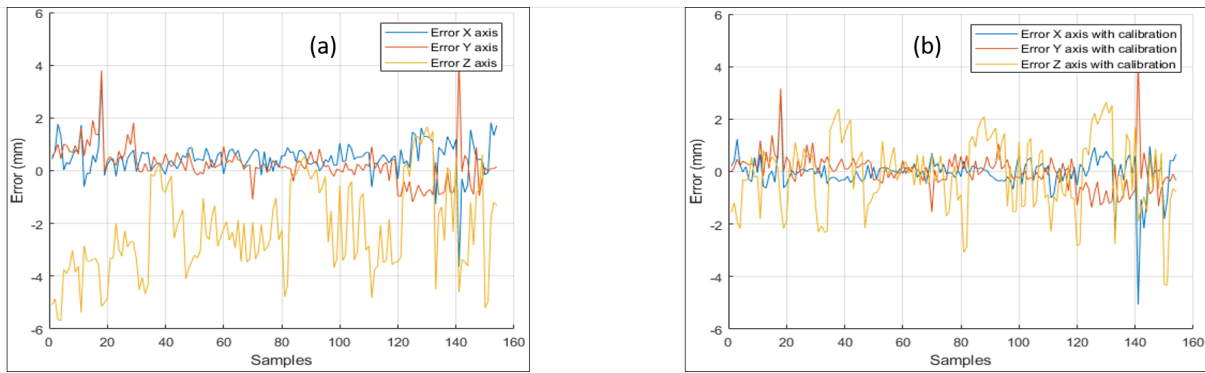


Fig. 17: (a) Error measures before calibration (b) Error measures after calibration.

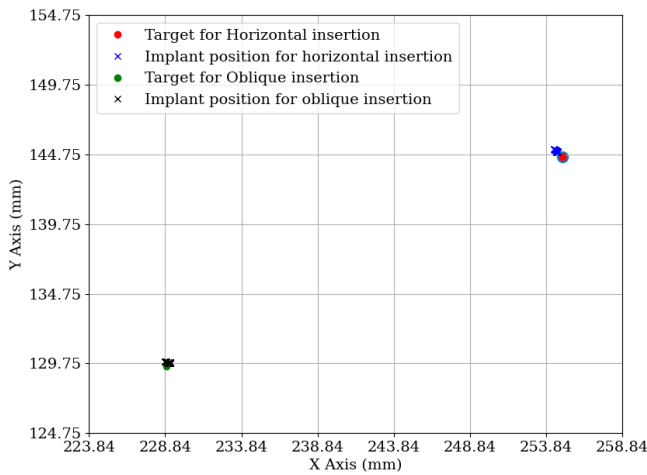


Fig. 18: Implant placement for horizontal and oblique insertions.

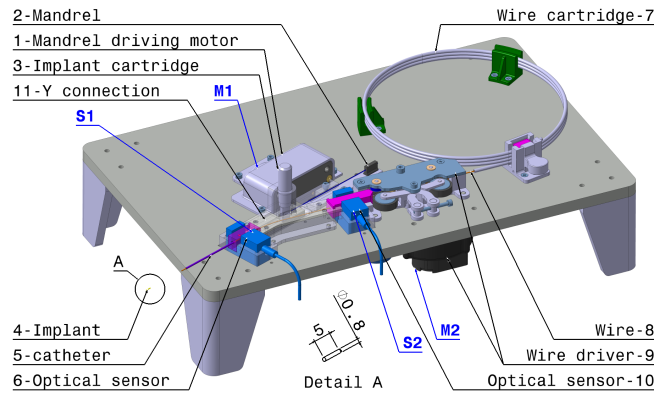


Fig. 19: CoBra implant driver

driven in translation by a USM motor (1) and by a rack and pinion system. The optical sensor (6) detects the end of the mandrel and the passage of the implant.

- 2) **Implant routing and deposit:** It is carried out by a cable (8) driven from the cartridge (7) by a system of motorized rollers (9). The drive system is equipped with an encoder to measure the deployed cable length. The optical sensor (10) is used to determine the end of the

cable. The cable guide track joins the pre-loading system track through a Y connection (11).

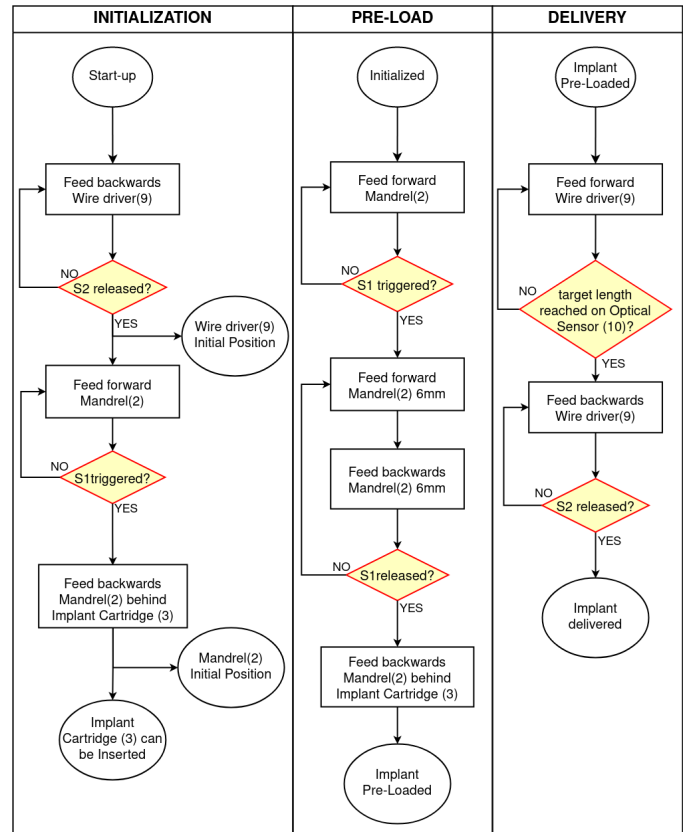


Fig. 20: Implant driver functioning flowchart

The flowchart for programming the automated driver Fig. (20) is divided into three following steps:

- 1) **Initialization step:** The program checks that the tracks are free and initializes the positions of the mandrel and the cable.
- 2) **Pre-loading step:** Motor M1 advances the mandrel (2) to the cartridge, extracts the implant from the cartridge, and advances to sensor S1 for detection of the presence of the implant, and the mandrel is advanced to the catheter entrance (5). Then the motor M1 retracts the mandrel (2) to its initial position.

- 3) **Delivery step:** Motor M2 drives the wire (8) to position S1 and unwinds the cable to the target. Once the implant deposition is validated by imaging, the wire¹⁴ is retracted to the position of S2.

VII. EXPERIMENTAL TESTS UNDER MRI ENVIRONMENT

The CoBra robot was tested in-bore under real-time MRI for velocity control, trajectory tracking, and component compatibility; with a bio-inspired phantom (BIP) at CHRU Lille Salengro hospital (Lille, FR) MR-facility (3T Philips Achieva dStream), and the CoBra setup and Implant driver at Philips R&D MR-facility (Best, NL). The CoBra team [26] developed an active prostate phantom made of silicon-based material to mimic the realistic dynamic targeting environment in terms of prostate deformation and inflammation (which occurs with multiple insertions), the setup is shown in Fig. 21 (Left column).

The MRI series used for real-time sequence - sBTfE_BH (TR/TE = 2.07/1.03 ms, slice thickness = 8 mm, complete metadata as supplementary file - S1). The MRI series used for images (shown in right column) in 21 - Turbo Spin Echo (TR/TE= 4800/90 ms ms, slice thickness = 3 mm, complete metadata as supplementary file - S2).

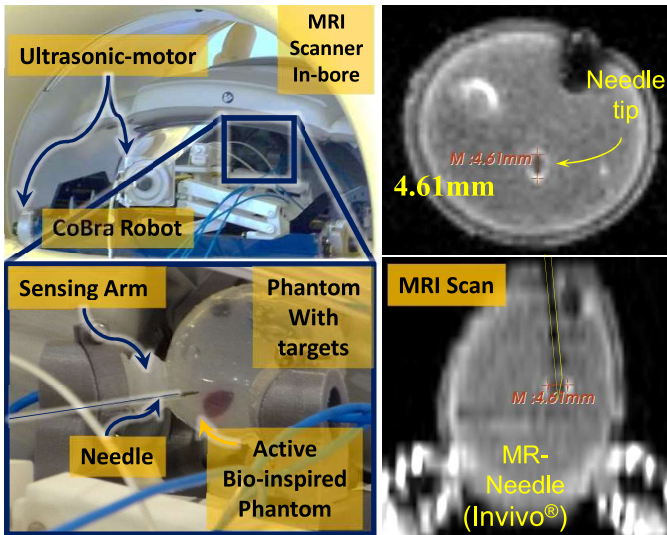


Fig. 21: Left: CoBra robot in-bore compatibility performance testing with BIP under MRI series - sBTfE_BH (refer to attached video), Right: BIP intervention under TSE Series.

In the following experimental tests, the authors present preliminary results of needle trajectory insertion and retraction inside a phantom in a 3T MRI environment. For these tests, the authors positioned the robot-guide to be near the isocentre, under the guidance of MRI. After position and velocity controls of T_{r1} , T_{r2} , T_{f1} , T_{f2} to reach this desired posture, the authors controlled in parallel the T_g linear axis in velocity using the piezo-motor and in position using a LAK14 310A prototype - glass ceramic scale absolute encoder. The functional compatibility of the robotic system has been

evaluated in-bore under real-time MRI (Philips 3T) at Roger Salengro Hospital in Lille. The MR-needle (Invivo - 18G) of Fig. 16 has been used to perform insertions by translating of module holding platform along the Z-axis. To evaluate the performance of the absolute sensor and the ultrasonic piezo-motor of the linear axis T_g , Fig. 22 indicates the control scheme for absolute position X^d and relative velocity \dot{X}^d under a 3T magnetic field. The PI controller parameters are: External Control PC (Proportional gain (Kp) = 0.7, Integral time (Ti) = 0.05) ; Motor controller (Proportional gain (Kp) = 0.5, Integral time (Ti) = 0.03), where the iteration time of the regulation loop is 0.05 s. The measurements are given by the absolute position sensor X^m and the absolute encoder for the velocity \dot{X}^m .

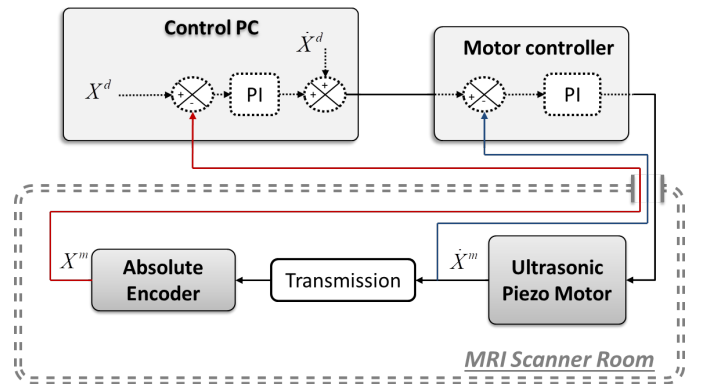


Fig. 22: Closed-loop position-velocity scheme of third linear axis T_g of the robot

Fig. 23 shows the T_g linear axis displacements with velocity variation under a 3T magnetic field. It is noticed that the profile of the measured velocity (dotted line) is close to the desired velocity (continue line), with low noises effect. The time x-label corresponds to the scan time.

Fig. 24 represents the tracking trajectory of the insertion and retraction of the needle inside the prostate phantom placed in-bore 3T MRI. These tests aim to verify the robustness of the closed-loop tracking of the driver needle system and to check the quality of the measurements of signals in in-bore 3T MRI.

The Fig. 25 shows the seed deposition on the test phantom. The phantom was prepared with MRI-visible markers (BioX-mark¹⁵, 75 μ L $\phi \approx 5.5$ mm) as an artificial target embedded in the EcoFlexTM Gel¹⁶. The markers were placed as an artificial targets in the grid pattern based on the conventional brachytherapy template used for needle placement but with limited entry points. Two seeds (IsoSeed® I-125 by BEBIG) were deposited using the CoBra implant driver under 3T MRI, Seed-1 (S1) to the Bioxmark(C7) and Seed-2 (S2) to open spot B7. Fig. 25 (Top) shows the placement of S1 within the BioXmark and the circle ($\phi = 5$ mm, marked for scale reference) at the C7 spot, and S2 deposited to an open spot at B7. It was observed from Fig. 25 that S1 was placed well with ≈ 2 mm accuracy inside the desired target and S2 at

¹⁴<https://www.marvistech.com/>

¹⁵<https://nanovi.com/bioxmark/introduction/>

¹⁶<https://www.smooth-on.com/products/ecoflex-gel/>

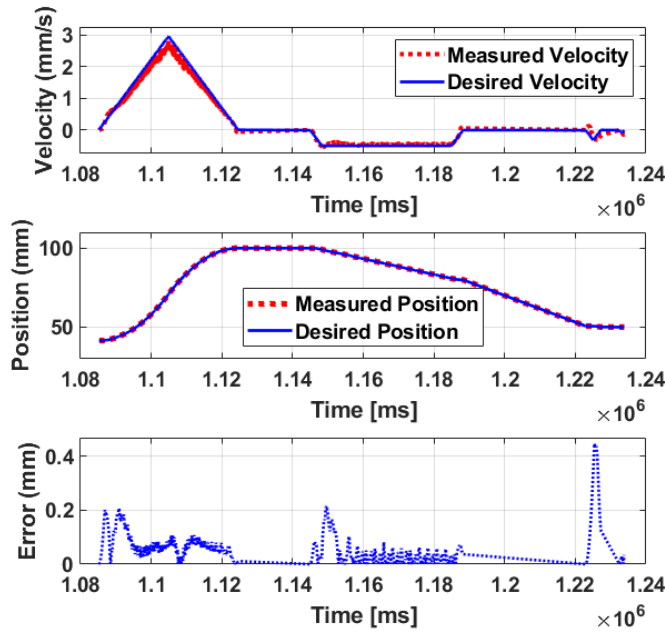


Fig. 23: Velocity variation of the T_g linear axis of the driver needle mechanism

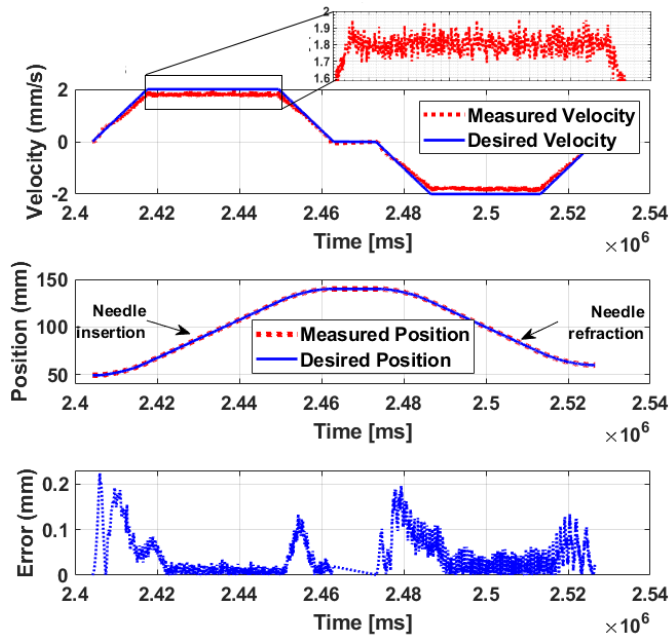


Fig. 24: Insertion and retraction of the needle

2.55mm from the pin-point target spot B7. Fig. 25 (Bottom-left) with an angled view shows the needle retraction trail (BioXmark liquid) and both deposited seeds. Fig. 26 shows the MRI scan of seed (S1) deposition under 3T (Ingenia Philips, Philips R&D center, NL), and MRI series - 3D FFE (TR/TE = 6.23/2.83, slice thickness = 1.2, complete metadata as supplementary file - S3). In preliminary results, the implant-driver showed promising outcomes with the robot.

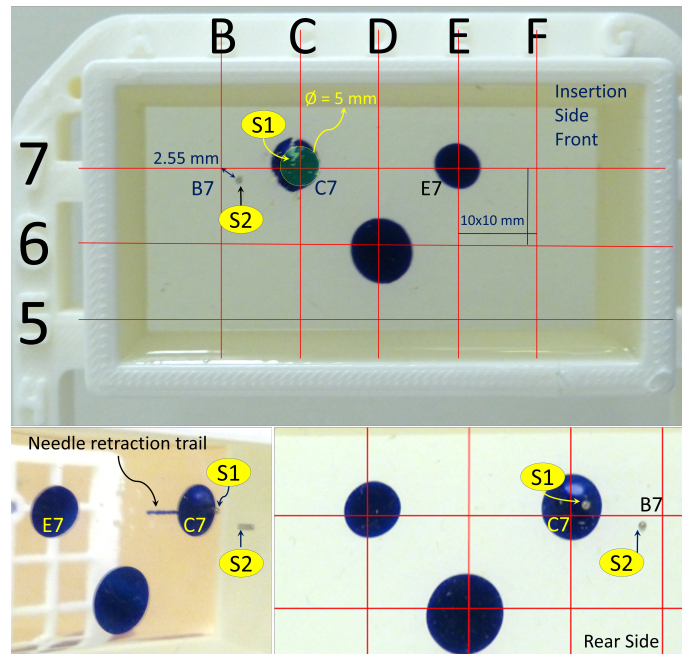


Fig. 25: Seed (S1 & S2) deposition with Implant driver.

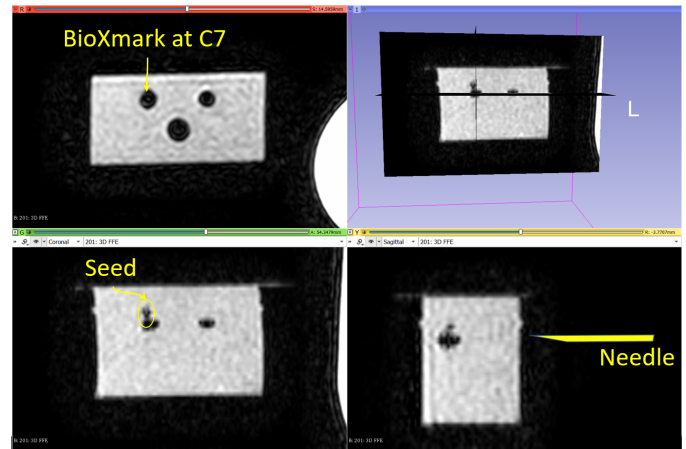


Fig. 26: MRI of deposited Seed (S1), 3D Slicer [43]

VIII. CONCLUSION AND FUTURE WORK

In this work, the authors introduced an integrated design of a 5-DOF MRI-conditional robot with an implant driver to perform LDR-Brachytherapy under real-time MRI without moving patients out of the MRI bore. It aims to perform adaptive BT, which accounts for the target shift due to soft-tissue local deformation and inflammation. The robot has the capacity to perform oblique insertions and doesn't need any template guide, thus targeting the prostate with minimally invasive access points. The tests and the kinematic model validation of the robot aimed to determine the in-bore functional compatibility of the actuators and sensors and the needle guidance under high magnetic fields in static and movement. The image clarity is promising with CoBra robot components actuating in-bore. The use of a new MR-conditional absolute sensor allows good quality of signal feedback to perform position closed-loop control. The needle insertion within the

bio-inspired prostate phantom also resulted in promising visual outcomes. The kinematic model calibration has allowed an accurate reconstruction of the needle tip pose. The results are close to the desired accuracy, although error sources such as needle bending during insertion or robot-to-patient registration are not taken into account in the current robot model. This issue will be investigated in future work by including the needle interaction model.

The CoBra concept, in the future steps, intends to develop a robotized adaptive prostate LDR-BT under MRI. To perform the MRI-adaptive LDR-BT, clinical workflow stages from diagnosis to post-implant quality assurance can be achieved with three sequential phases: Pre-treatment, Treatment, and Post-treatment phase, as shown in Fig. 27. Further, these phases can be divided into sub-tasks combining software and hardware for the robotized concept.

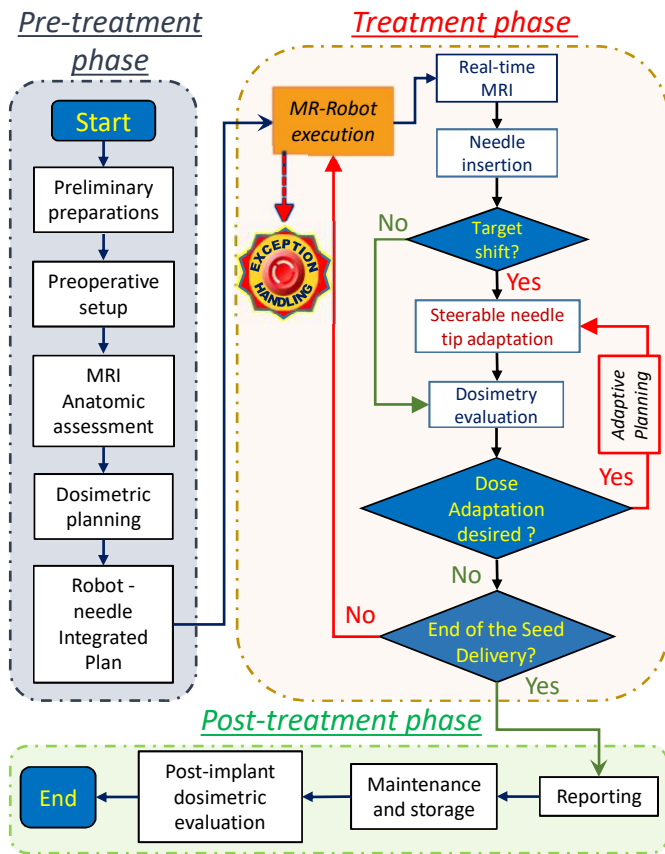


Fig. 27: CoBra MRI Adaptive-BT Workflow.

Pre-treatment phase: In this phase, based on anatomic assessment, dose calculation and planning, *Dosimetry* is performed, and for robot control and needle trajectory guidance, *Robot planning* is performed.

Treatment phase: The main phase of the LDR-BT procedure is where the execution of needle insertion under real-time MRI is carried out with the robot's help. Needle trajectories can be updated, and consequently, adapt to dose calculation and dose delivery to overcome the shifted target problem. Adaptive MR-based control of the CoBra needle guide robot along with the detectable changes in the prostate target position during the intervention.

Post-treatment phase: Accounts for the post-implant dosimetric evaluation. Additional images can be acquired to verify that the LDR-BT plan was successfully executed and assist in post-treatment follow-up.

The CoBra (*Cooperative Brachytherapy*) can be defined as direct robotized control guidance of needle insertion. Ensuring the needle insertion follows the desired trajectory and updating it simultaneously. The treatment phase is to be performed intraoperatively under MRI without moving the patient outside the scanner, ensuring stable position, updating, and verifying implant delivery according to the adaptive dosimetry. Adaptive dosimetry accounts for relative implant positioning and confirms the dose to lesion the site using a steerable needle.

ACKNOWLEDGMENT

Authors thank partners and observers for assisting with components, TPS by *Eckert & Ziegler BEBIG GmbH*, Uni-Lift by *NORAS MRI products GmbH*, MR-guidewire by *MaR-VisTech GmbH*, flexible catheter by *Zeus*, MRI-conditional camera by *MRC-systems GmbH*, and BioXmark by *Nanovi*. Authors would also like to thank Mr. Jouke Smink, PhD for assisting in MRI tests at the Dept. of Clinical Research, Philips Healthcare, Best, NL.

REFERENCES

- [1] T. K. Podder, L. Beaulieu, B. Caldwell, R. A. Cormack, J. B. Crass, A. P. Dicker *et al.*, "AAPM and GEC-ESTRO guidelines for image-guided robotic brachytherapy: Report of Task Group 192," *Medical Physics*, vol. 41, no. 10, 2014.
- [2] A. D'Amico, R. Cormack, C. Tempny, S. Kumar, G. Topulos, H. Kooy, and C. N. Coleman, "Real-time magnetic resonance image-guided interstitial brachytherapy in the treatment of select patients with clinically localized prostate cancer," *International Journal of Radiation Oncology • Biology • Physics*, vol. 42, no. 3, pp. 507–515, 1998.
- [3] N. Tsekos, A. Khanicheh, E. Christoforou, and C. Mavroidis, "Magnetic resonance-compatible robotic and mechatronics systems for image-guided interventions and rehabilitation: a review study," *Annual Review of Biomedical Engineering*, vol. 9, pp. 351–87, 2007.
- [4] R. Monfaredi, K. Cleary, and K. Sharma, "MRI robots for needle-based interventions: systems and technology," *Annals of Biomedical Engineering*, vol. 46, no. 10, pp. 1479–1497, 2018.
- [5] S. S. Dhaliwal, T. Chettibi, S. Wilby, W. Polak, A. L. Palmer, N. Reynaert, and R. Merzouki, "Review of Clinical and Technological Consideration for MRI-Guided Robotic Prostate Brachytherapy," *IEEE Transactions on Medical Robotics and Bionics*, vol. 3, no. 3, pp. 583–605, 2021.
- [6] S. P. DiMaio, S. D. Pieper, K. Chinzei, N. Hata, S. Haker, D. F. Kacher, G. Fichtinger, C. M. Tempny, and R. Kikinis, "Robot-assisted needle placement in open MRI: system architecture, integration and validation," *Computer aided surgery : official journal of the International Society for Computer Aided Surgery*, vol. 12 1, pp. 15–24, 2006.
- [7] M. Muntener, A. Patriciu, D. Petrisor, M. Schar, D. Ursu, D. Y. Song, and D. Stoianovici, "Transperineal prostate intervention: robot for fully automated MR imaging—system description and proof of principle in a canine model," *Radiology*, vol. 247, no. 2, pp. 543–549, 2008.
- [8] M. R. Van den Bosch, M. R. Moman, M. Van Vulpen, J. J. Battermann, E. Duiveman *et al.*, "MRI-guided robotic system for transperineal prostate interventions: proof of principle," *Physics in Medicine & Biology*, vol. 55, no. 5, p. N133, 2010.
- [9] A. Krieger, I. I. Iordachita, P. Guion, A. K. Singh, A. Kaushal, C. Ménard *et al.*, "An MRI-compatible robotic system with hybrid tracking for MRI-guided prostate intervention," *IEEE Transactions on Biomedical Engineering*, vol. 58, no. 11, pp. 3049–3060, 2011.
- [10] G. Miron, A. Girard, J.-S. Plante, and M. Lepage, "Design and Manufacturing of Embedded Air-Muscles for a Magnetic Resonance Imaging Compatible Prostate Cancer Binary Manipulator," *Journal of Mechanical Design*, vol. 135, no. 1, 11 2012, 0111003. [Online]. Available: <https://doi.org/10.1115/1.4007932>

- [11] G. Li, H. Su, W. Shang, J. Tokuda, N. Hata, C. M. Tempny, and G. S. Fischer, "A fully actuated robotic assistant for MRI-guided prostate biopsy and brachytherapy," *Medical Imaging 2013: Image-Guided Procedures, Robotic Interventions, and Modeling*, vol. 8671, p. 867117, 2013.
- [12] S. Jiang, J. Guo, S. Liu, J. Liu, and J. Yang, "Kinematic analysis of a 5-dof hybrid-driven mr compatible robot for minimally invasive prostatic interventions," *Robotica*, vol. 30, no. 7, pp. 1147–1156, 2012.
- [13] P. Moreira, G. van de Steeg, T. Krabben, J. Zandman, E. E. Hekman, F. van der Heijden, R. Borra, and S. Misra, "The MIRIAM Robot: A Novel Robotic System for MR-Guided Needle Insertion in the Prostate," *Journal of Medical Robotics Research*, vol. 2, pp. 1750006:1–1750006:13, 2017.
- [14] R. Seifabadi, S.-E. Song, A. Krieger, N. B. Cho, J. Tokuda, G. Fichtinger, and I. Iordachita, "Robotic system for MRI-guided prostate biopsy: feasibility of teleoperated needle insertion and ex vivo phantom study," *International Journal of Computer Assisted Radiology and Surgery*, vol. 7, pp. 181–190, 2011.
- [15] N. A. Patel, G. Li, W. Shang, M. Wartenberg, T. Heffter, E. Burdette, I. Iordachita, J. Tokuda, N. Hata, C. Tempny, and G. Fischer, "System Integration and Preliminary Clinical Evaluation of a Robotic System for MRI-Guided Transperineal Prostate Biopsy," *Journal of Medical Robotics Research*, vol. 4 2, 2019.
- [16] H. Elhawary, Z. T.-H. Tse, M. Rea, A. Zivanovic, B. L. Davies, C. Besant, N. De Souza, D. Mcrobbie, I. Young, and M. Lamperth, "Robotic system for transrectal biopsy of the prostate: real-time guidance under MRI," *IEEE Engineering in Medicine and Biology Magazine*, vol. 29, no. 2, pp. 78–86, 2010.
- [17] A. A. Goldenberg, J. Trachtenberg, Y. Yi, R. Weersink, M. S. Sussman, M. Haider, L. Ma, and W. Kucharczyk, "Robot-assisted MRI-guided prostatic interventions," *Robotica*, vol. 28, no. 2, p. 215–234, 2010.
- [18] Y. Lin, Y. Shi, J. Zhang, F. Wang, W. Wu, and H. chao Sun, "Design and control of a piezoelectric actuated prostate intervention robotic system*," *2020 17th International Conference on Ubiquitous Robots (UR)*, pp. 175–180, 2020.
- [19] A. Martin, G. Miron, F. Thérien, C. Véronneau, D. Bouchard, and J. S. Plante, "Robotically Guided Prostatic Fiducial Marker Insertion Under Direct MRI Guidance: A Proof of Concept in a Live Canine Subject," *International Journal of Radiation Oncology • Biology • Physics*, vol. 90, 2014.
- [20] J. Wang, K. Tanderup, A. Cunha, A. L. Damato, N. C. Gil'ad, R. J. Kudchadker, and F. Mourtada, "Magnetic resonance imaging basics for the prostate brachytherapist," *Brachytherapy*, vol. 16, no. 4, pp. 715–727, 2017.
- [21] D. S. Stoianovici, C. Kim, D. Petrisor, C. Jun, S. Lim, M. W. Ball, A. E. Ross, K. J. Macura, and M. E. Allaf, "MR Safe Robot, FDA Clearance, Safety and Feasibility of Prostate Biopsy Clinical Trial," *IEEE/ASME Transactions on Mechatronics*, vol. 22, pp. 115–126, 2017.
- [22] P. Moreira, N. Patel, M. Wartenberg, G. Li, K. Tuncali, T. Heffter, E. C. Burdette, I. Iordachita, G. S. Fischer, N. Hata *et al.*, "Evaluation of robot-assisted mri-guided prostate biopsy: needle path analysis during clinical trials," *Physics in Medicine & Biology*, vol. 63, no. 20, p. 20NT02, 2018.
- [23] C. Rossa and M. Tavakoli, "Issues in closed-loop needle steering," *Control Engineering Practice*, vol. 62, pp. 55–69, 2017.
- [24] S. S. Dhaliwal, T. Chettibi, A. Belarouci, G. Dherbomez, V. Coelen, and R. Merzouki, "Cooperative Brachytherapy for Prostate Cancer Under MRI Guidance," *2019 Fifth International Conference on Advances in Biomedical Engineering (ICABME)*, pp. 1–4, 2019. [Online]. Available: <https://doi.org/10.1109/ICABME47164.2019.8940278>
- [25] S. S. Dhaliwal, S. Wilby, S. Firouzy, K. B. Boni, M. de Vries, S. E. Navarro, A. Belarouci *et al.*, "CoBra robot for localized cancer treatment and diagnosis under real-time MRI," *AUTOMED 2021*, June 2021. [Online]. Available: <http://doi.org/10.5281/zenodo.4923036>
- [26] S. E. Navarro, S. S. Dhaliwal, M. S. Lopez, S. Wilby, A. L. Palmer, W. Polak, R. Merzouki, and C. Duriez, "A Bio-Inspired Active Prostate Phantom for Adaptive Interventions," *IEEE Transactions on Medical Robotics and Bionics*, pp. 1–1, 2021.
- [27] T. Hellebust, "Place of modern imaging in brachytherapy planning," *Cancer/Radiothérapie*, vol. 22, no. 4, pp. 326–333, 2018.
- [28] F. A. Jolesz, "Intraoperative imaging and image-guided therapy," *Springer*, pp. –, 2014.
- [29] A. N. Viswanathan, J. Dimopoulos, C. Kirisits, D. Berger, and R. Pötter, "Computed tomography versus magnetic resonance imaging-based contouring in cervical cancer brachytherapy: results of a prospective trial and preliminary guidelines for standardized contours," *International Journal of Radiation Oncology* Biology* Physics*, vol. 68, no. 2, pp. 491–498, 2007.
- [30] M. De Brabandere, P. Hoskin, K. Haustermans, F. Van den Heuvel, and F.-A. Siebert, "Prostate post-implant dosimetry: interobserver variability in seed localisation, contouring and fusion," *Radiotherapy and Oncology*, vol. 104, no. 2, pp. 192–198, 2012.
- [31] A. Dohan, C. Hoeffel, P. Soyer, A. Jannot, P. Valette, A. Thivolet, G. Passot, O. Glehen, and P. Rousset, "Evaluation of the peritoneal carcinomatosis index with ct and mri," *Journal of British Surgery*, vol. 104, no. 9, pp. 1244–1249, 2017.
- [32] D. S. Stoianovici, C. Kim, G. Srimathveeravalli, P. Sebrect, D. Petrisor, J. A. Coleman, S. B. Solomon, and H. Hricak, "MRI-Safe Robot for Endorectal Prostate Biopsy," *IEEE/ASME Transactions on Mechatronics*, vol. 19, pp. 1289–1299, 2013.
- [33] A. Fedorov, K. Tuncali, F. Fennessy, J. Tokuda, N. Hata, W. M. Wells, R. Kikinis, and C. M. C. Tempny, "Hierarchical Image Registration for Improved Sampling During 3T MRI-Guided Transperineal Targeted Prostate Biopsy," 19th Annual meeting & Exhibition ISMRM, <https://archive.ismrm.org/2011/3055.html>, May 2011.
- [34] S. Eslami, G. S. Fischer, S.-E. Song, J. Tokuda, N. Hata, C. M. Tempny *et al.*, "Towards clinically optimized MRI-guided surgical manipulator for minimally invasive prostate percutaneous interventions: constructive design," *2013 IEEE International Conference on Robotics and Automation*, pp. 1228–1233, 2013.
- [35] W. Wang, Y. Shi, X. Yuan, A. Goldenberg, and P. Shokrollahi, "Compatibility of US motors for development of MRI-guided surgical robot," *2013 6th International Conference on Biomedical Engineering and Informatics*, pp. 388–392, 2013.
- [36] P. Shokrollahi, J. M. Drake, and A. A. Goldenberg, "Signal-to-noise ratio evaluation of magnetic resonance images in the presence of an ultrasonic motor," *Biomedical Engineering Online*, vol. 16, no. 1, p. 45, 2017.
- [37] K.-Y. Kim, M. Li, B. Gonenc, W. Shang, S. Eslami, and I. Iordachita, "Design of an MRI-compatible modularized needle driver for in-bore MRI-guided prostate interventions," *2015 15th International Conference on Control, Automation and Systems (ICCAS)*, pp. 1520–1525, 2015.
- [38] P. Li, Z. Yang, and S. Jiang, "Needle-tissue interactive mechanism and steering control in image-guided robot-assisted minimally invasive surgery: a review," *Medical & Biological Engineering & Computing*, vol. 56, no. 6, pp. 931–949, 2018.
- [39] A. Patriciu, D. Petrisor, M. Muntener, D. Mazilu, M. Schar, and D. Stoianovici, "Automatic brachytherapy seed placement under MRI guidance," *IEEE Transactions on Biomedical Engineering*, vol. 54, no. 8, pp. 1499–1506, 2007.
- [40] R. Merzouki, V. Coelen, E. Lartigau, and A. Belarouci, "AUTONOMOUS GUIDANCE SYSTEM FOR NEEDLE-HOLDING EQUIPMENT," France Patent WO2017009572, January 19, 2017.
- [41] M. Sato, Y. Saito, T. Takayama, T. Omata, H. Watanabe, R. Yoshimura, and M. Miura, "Remote radioactive seed-loading device for permanent brachytherapy of oral cancer with Au-198 grains," *ROBOMECH Journal*, vol. 4, pp. 1–10, 2017.
- [42] J. A. Proffitt and A. K. Ball, "A Device for the Automated Loading and Detection of Brachytherapy Elements Using Nonmechanical Methods for use in Prostate Cancer Treatment," *Journal of Medical Devices-Transactions of The ASME*, vol. 6, p. 021009, 2012.
- [43] A. Fedorov, R. Beichel, J. Kalpathy-Cramer, J. Finet, J.-C. Fillion-Robin, S. Pujol, C. Bauer, D. Jennings, F. Fennessy, M. Sonka *et al.*, "3D Slicer as an image computing platform for the Quantitative Imaging Network," *Magnetic Resonance Imaging*, vol. 30, no. 9, pp. 1323–1341, 2012.